RSC Advances

PAPER

View Article Online
View Journal | View Issue

Cite this: *RSC Adv.*, 2021, **11**, 39130

A highly stable and sensitive ethanol sensor based on Ru-decorated 1D WO_3 nanowires†

Jianjun Li,[a] Qiongling Ding,[a] Xichao Mo,[a] Zihao Zou,[b] Pu Cheng,[b] Yiding Li,[b] Kai Sun,[b] Yujun Fu,[b] Yanrong Wang *[a] and Deyan He[b]

Received 3rd September 2021
Accepted 20th November 2021

DOI: 10.1039/d1ra06623d

rsc.li/rsc-advances

Decorating materials with noble metal catalysts is an effective method for optimizing the sensing performance of sensors based on tungsten trioxide (WO_3) nanowires. Ruthenium (Ru) exhibits excellent catalytic activity for oxygen adsorption/desorption and chemical reactions between gases and adsorbed oxygen. Herein, small Ru nanoparticles were uniformly distributed on the surface of one-dimensional WO_3 nanowires. The nanowires were prepared by the electrospinning method through an ultraviolet (UV) irradiation process, and decoration with Ru did not change their morphology. A sensor based on 4% Ru nanowires (NWs) shows the highest response (~120) to 100 ppm ethanol, which was increased around 47 times, and the lowest ethanol detection limit (221 ppb) at a lower temperature (200 °C) displays outstanding repeatability and stability even after 45 days or in higher-humidity conditions. Moreover, it also has faster response–recovery features. The improvement in the sensing performance was attributed to the stable morphology of the nanowires, the sensitization effect of Ru, the catalytic effect of RuO_2 and the optimal atomic utilization efficiency. This work offers an effective and promising strategy for promoting the ethanol sensing performance of WO_3.

1 Introduction

The electrical properties of metal oxide semiconductors (MOS) are related to the ambient atmosphere, and they have the features of low cost, robustness, and easy synthesis.[1–3] Thus, they play a significant role in gas sensing applications to detect toxic, inflammable and explosive gases,[4–6] and are more favored by scientific researchers compared to sensors based on metamaterials[7–10] or nanophotonics.[11–13] MOS-based sensors have been reported over the past several decades, including sensors based on CuO,[14] SnO_2,[15] In_2O_3,[16] Co_3O_4,[17] Fe_2O_3,[18] ZnO,[19] and NiO,[20] for applications such as monitoring air quality and ensuring industrial safety. The discharge and leakage of volatile organic compounds (VOCs) into the environment are inevitable because of the limitations of current production technology. There is significant harm to human health when people live in an environment with VOC gases.[21–23] Thus, it is of great concern to design devices, such as sensors based on complementary infrared ray metamaterials, for the purpose of detecting VOCs.[24] Ethanol is a typical flammable and volatile colorless transparent liquid at normal temperature and pressure, and is widely used in national defense, the chemical industry, medicine and healthcare, the food industry, and industrial and agricultural production.[25,26] In particular, ethanol vapor can form an explosive mixture with air, and it is also an inhibitor of the central nervous system.[27] Therefore, from a human health perspective, many efforts to improve the properties of sensors for monitoring ethanol are urgently needed.

Tungsten trioxide (WO_3), with a morphology that is easily controlled through various synthesis methods, is an n-type MOS material[28] and displays good gas sensitivity in the detection of NO_2,[29] xylene,[30] methanol,[31] and acetone.[32] Based on the typical gas sensing mechanism of MOS materials,[33] various methods for optimizing the sensing performance of WO_3-based sensors have been studied. These include different methods such as morphology control,[34] heterostructure construction,[35] defect introduction,[36] and metal doping or decoration. Among these methods, using noble metals (Au,[37] Pd,[38] Pt[39]) to decorate the MOS material surface is considered to be a promising strategy to boost its sensing performance due to their catalytic properties, sensitization effect, or spillover effect. However, the long-term stability of sensors prepared through the functional modification of the surface of WO_3 is usually poor. Generally, a sensing material should provide sufficient reaction sites between the target gas and adsorbed oxygen, meaning that the materials need a large specific surface area; therefore, nanomaterials are regarded as good candidate materials for fabricating sensors.

Electrospinning has become one of the main ways to effectively prepare nanomaterials due to the simple and controllable

[a]School of Physical Science and Technology, Lanzhou University, Lanzhou 730000, China. E-mail: wyr@lzu.edu.cn

[b]School of Materials and Energy, Lanzhou University, Lanzhou 730000, China

† Electronic supplementary information (ESI) available. See DOI: 10.1039/d1ra06623d

manufacturing process, low cost, and the wide range of spinnable materials.[40,41] Electrospun nanowires have a high specific surface area and porosity, which increases the area of interaction between the sensing material and the target object. Therefore, electrospun nanomaterials are expected to significantly improve the performance of gas sensors.[42,43] Ruthenium (Ru) is a relatively inexpensive noble metal with stable properties and strong corrosion resistance, and it has been reported as an effective catalyst for the hydrogen evolution reaction[44] and conversion of VOCs.[45] Ascribed to its favorable electronic properties, the introduction of Ru can promote the formation of oxygen-containing species adsorbed on the surface of materials and effectively break C–C bonds, which improves the chemical reaction between ethanol and adsorbed oxygen.[46–48] In addition, ethoxy species of ethanol are always present as monodentates with their oxygen atom bound to one Ru atom.[49] In recent years, there has been no shortage of published articles on Ru doping or the modification of MOS materials to optimize the gas sensing performance of MOS-based sensors.[50,51] Thus, Ru decoration methods may promote ethanol sensing performance.

Based on the above discussion, in this work, 1D WO_3 nanowires (NWs) were prepared through a traditional electrospinning method. Ru catalyst particles were successfully decorated on the surface of the WO_3 NWs through a UV irradiation process with tungstic acid and ruthenium chloride hydrate as the raw materials. Sensors based on 4% Ru loaded on WO_3 show an outstanding response, rapid response and recovery, and excellent selectivity to ethanol. The introduction of Ru also decreases the optimum working temperature of the sensor. Furthermore, the effect of moisture and the long-term stability of these sensors were also studied. The results obtained herein clearly demonstrate that decorating the surface of WO_3 NWs with a moderate amount of Ru is an effective and promising method for promoting ethanol-sensing performance.

2 Experimental section

2.1 Preparation of pure WO_3 nanowires

All the relevant chemicals used in this work were of analytical grade and were used directly without purification. Deionized (DI) water with a resistivity of 18.25 MΩ cm was used in all synthesis and fabrication processes. The WO_3 NWs were prepared by an optimized traditional electrospinning method followed by an annealing process using tungstic acid as a precursor following a modified method reported previously.[52] The preparation of pure WO_3 nanowires (NWs) is shown schematically in Fig. 1a. Briefly, 1.7 g polyvinylpyrrolidone (PVP, average MW ~1 300 000) was placed in a bottle with a mixed solvent containing 5 mL absolute ethanol and 2 mL DI water. This mixture was vigorously stirred for 5 h. 4 mL ammonia was poured into a bottle with 390 mg tungstic acid. This bottle was placed in a 65 °C water bath and stirred for 2 h. The ammonia solution was then slowly poured into the PVP solution and stirred constantly overnight. The obtained milky white precursor solution was then drawn into a plastic syringe. The parameters of the electrospinning process were set as follows: an applied voltage of 19 kV, a feed rate of 0.2 mL h^{-1}, and a working distance of 20 cm. The obtained precursor wires were preoxidized at 200 °C for 2 h and annealed at 500 °C for 2 h in a muffle furnace with a heating rate of 1 °C min^{-1} to remove the PVP. The samples were cooled to 300 °C with a cooling rate of 2 °C min^{-1}, followed by natural cooling to room temperature to obtain pure WO_3 NWs, denoted as 0% Ru NWs.

2.2 Preparation of Ru-decorated WO_3 nanowires

For the Ru-decorated samples, various atomic concentrations of Ru (at% = 2, 3, 4, 5, and 6) were used to functionalize the surface of the WO_3 NWs *via* a UV irradiation process. In a typical process, 30 mg 0% Ru NWs were dispersed in 9 mL DI water under ultrasonic agitation for 15 min. The corresponding amount of ruthenium chloride hydrate ($RuCl_3$, 0.02 M) aqueous solution was added dropwise at 500 rpm. The solution was stirred at 500 rpm for 5 min and then at 1000 rpm for 10 min. UV irradiation was then performed at 300 rpm for 5 h. The products were centrifuged at 8000 rpm for 4 min and washed with DI water and absolute ethanol several times. Finally, the samples were dried at 60 °C for 12 h. The corresponding samples were denoted as 2, 3, 4, 5, and 6% Ru NWs.

2.3 Sensor fabrication and measurement

The gas sensing performance of the samples was measured using a WS-30B gas sensing measurement system (Wei-Sheng Electronics Co., Ltd, China). First, a small amount of each prepared powder (0.7 mg for each device) was mixed with an appropriate amount of a laboratory-made organic binder containing 10 wt% ethyl cellulose and 90 wt% terpineol. Each mixture was ground to form a paste, which was uniformly coated onto the surface of a ceramic tube with a pair of Au electrodes and four Pt wires; it is clear that the thickness of the sample coating layer is about 14 μm from the cross-sectional view SEM image of the sensor device shown in Fig. 1d. To completely remove the organic binder, a calcination process was carried out at 400 °C for 2 h in a muffle furnace. A Ni–Cr wire coil heater was inserted into the tubes to regulate the working temperature of the sensor devices by the providing the corresponding heating voltage (V_h). A schematic of the device is shown in Fig. 1b. For the purpose of obtaining good stability, the devices were aged at 200 °C for 36 h prior to testing. To determine the sensing performance of the sensors, all the devices were placed in a test chamber with an 18 L capacity and tested under ambient conditions (30 °C, 35 RH%). The devices were then preheated to various temperatures (110–230 °C) for about 0.5 h. At this point, when the electrical resistance values of the devices (R_a and R_g, which represent the resistances in air and in the presence of target gases, respectively) were stable, using the experimental setup shown in the schematic illustration in Fig. 1c, the resistance value of the devices was calculated using the formula: R_a (or R_g) = $(V_c - V_{out}) \times R_L/V_{out}$, (the value of V_c or R_L was a known constant, V_{out} was obtained from the WS-30B gas sensing measurement system), a corresponding volume of the target gas was injected into the test chamber using a microinjector, and fans were used to accelerate gas

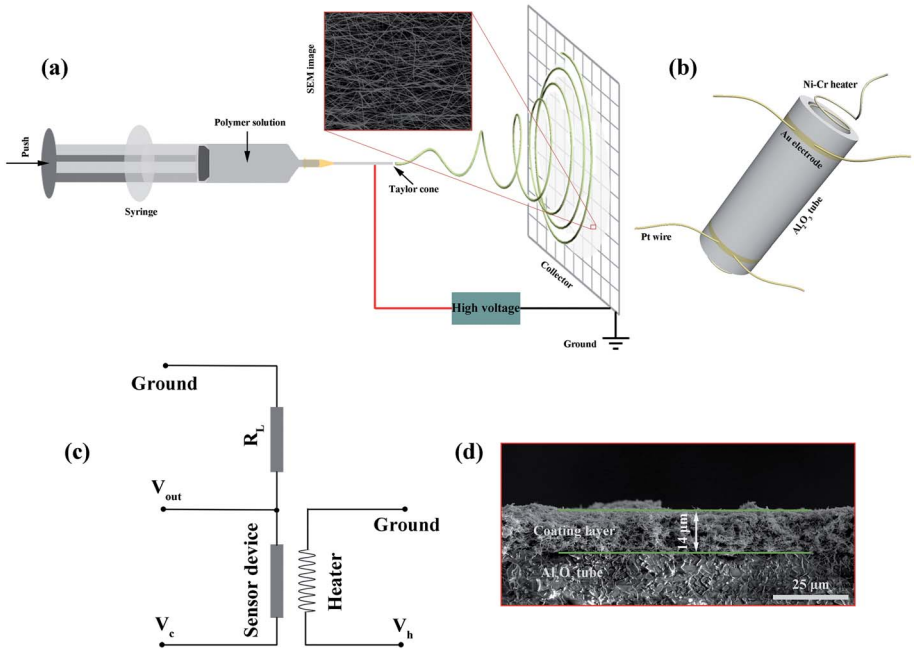

Fig. 1 (a) Schematic illustration showing preparation of WO_3 NWs by electrospinning, (b) the ceramic tube device, (c) schematic illustration of the experimental setup, and (d) cross-sectional view SEM image of the sensor device.

dispersion. The response value S is defined as $S = R_a/R_g$. Furthermore, the response and recovery times (τ_{res} and τ_{rec}) are defined as the time required for the value of the resistance to change by 90%.

2.4 Characterization

The structures, morphologies, and elemental compositions of the samples were characterized using field-emission scanning electron microscopy (FE-SEM, FEI Apreo-S), transmission electron microscopy (TEM, FEI Tecnai F30, operated at 300 kV), and energy-dispersive X-ray spectroscopy (EDS). X-ray powder diffraction (XRD, Malvern Panalytical) with Cu-Kα radiation (λ = 1.5406 Å) at 40 kV and 40 mA, as well as micro-Raman spectroscopy (Renishaw inVia-Reflex with an excitation wavelength of 785 nm) was used to analyze the crystalline phase structure and composition of the samples. The surface elemental chemical states of the samples were analyzed using X-ray photoelectron spectroscopy (XPS, Kratos Axis Ultra DLD with Al Kα probe beam). The C 1s peak (284.6 eV) was used as a reference for element binding energy calibration.

3 Results and discussion

3.1 Structural and morphological characteristics

The XRD patterns of the pure and Ru-decorated WO_3 NWs sample are shown in Fig. 2a, demonstrating the good crystallinity of all the samples, which were well-indexed to the monoclinic structure of WO_3 (JCPDS card no. 72-0677). The main peaks located at 2θ = 23.11°, 23.58°, and 24.35° correspond to the (0 0 2), (0 2 0) and (2 0 0) lattice planes of WO_3,

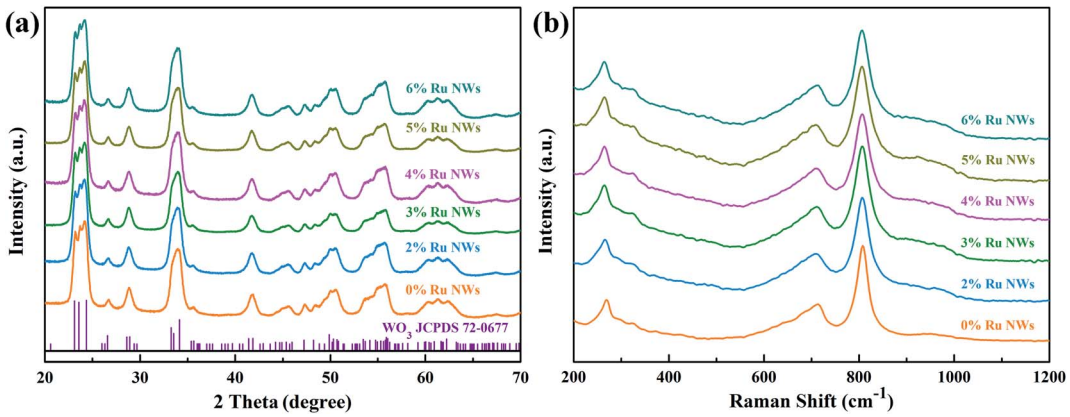

Fig. 2 (a) XRD patterns and (b) Raman spectra of 0%, 2%, 3%, 4%, 5%, and 6% Ru NWs.

respectively.[52] No additional diffraction peaks corresponding to trace ruthenium or impurity phases were detected. The Raman spectra of the as-prepared samples are presented in Fig. 2b to further confirm their molecular structure information, and they illustrate that all the samples have similar spectra. The intense Raman peaks at shifts of 271 cm^{-1}, 328 cm^{-1} and 715 cm^{-1}, and 807 cm^{-1} can be assigned to the O–W–O bending vibration and stretching vibration modes of monoclinic-phase WO_3,[50] respectively. Overall, the XRD and Raman characterizations illustrate that the modification of the WO_3 NWs with a trace amount of noble metals does not affect their crystal phase or molecular structure.

The microstructures of as-prepared pure and Ru-loaded WO_3 NW samples were observed through SEM and TEM images. Fig. 3a–f show that the rough and porous nanowires have a uniform diameter of about 100 nm, are constructed from a large number of WO_3 nanoparticles, and exhibit a net structure of nanowires leading to a large mesoporous structure. This structure is beneficial for gas diffusion processes and achieving a highly sensitive response, because it has a high number of gas reaction and adsorption sites and is conducive to the diffusion or overflow of the surface of the materials.[53] A comparison of the SEM images of the different samples shows that there is no difference in their morphology. The ruthenium loading level is very low, beyond the resolution limitation of SEM, but the images indicate that the presence of Ru does not affect the microstructure of the nanowires, in line with the XRD and Raman results. Furthermore, the TEM images shown in Fig. 4a and b also show that the 0% Ru NWs and 4% Ru NWs have a diameter of about 100 nm and are formed of many small WO_3 nanoparticles even after Ru decoration. Fortunately, comparison of the TEM image of the 4% Ru NWs in Fig. 4b with the image obtained from the 0% Ru NWs shows that there are abundant Ru nanoparticles with a size of several nanometers loaded on the surface of the WO_3 nanoparticles.

The high-resolution transmission electron microscope (HRTEM) images of the samples shown in Fig. 4c and d present the lattice information, with interplanar distances of 0.335 nm, 0.356 nm, 0.39 nm, and 0.256 nm, which can be ascribed to the (1 2 0), (2 0 0), and (0 0 1) planes of monoclinic phase WO_3 and the (1 0 1) planes of RuO_2, respectively.[21,51] The STEM image and corresponding EDS elemental mapping shown in Fig. 4e–h prove that W, O, and Ru are uniformly distributed in the 4% Ru NW sample. These results indicate that Ru is successfully decorated on the WO_3 NWs and mainly exists in the form of RuO_2.

3.2 Gas sensing performance

Determining the working temperature of sensor devices is very important for their practical application. In particular, achieving a low working temperature for sensors based on MOS is important to reduce power consumption and the risk of combustion or explosion when monitoring ethanol gas. Therefore, the relationship between the response of the sensor devices to 100 ppm ethanol over an operating temperature range of 110–230 °C was investigated, as shown in Fig. 5a. Clearly, the response values of the devices based on samples decorated with Ru increase as the working temperature

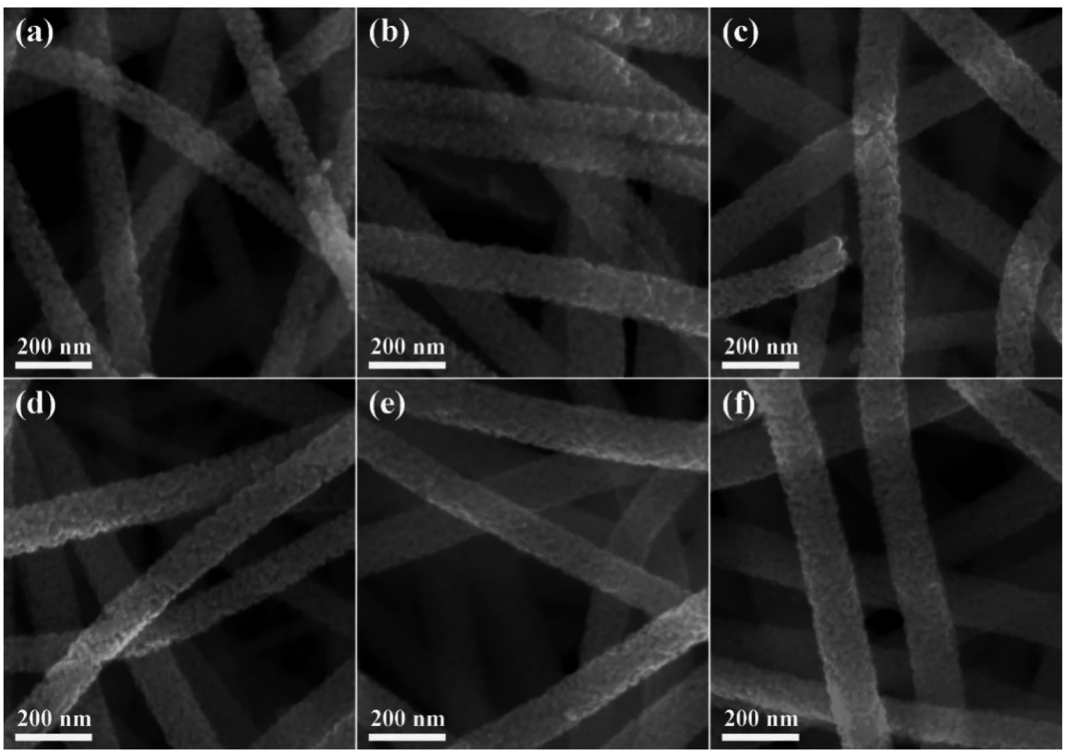

Fig. 3 SEM images of different samples: (a) 0% Ru NWs; (b) 2% Ru NWs; (c) 3% Ru NWs; (d) 4% Ru NWs; (e) 5% Ru NWs; (f) 6% Ru NWs.

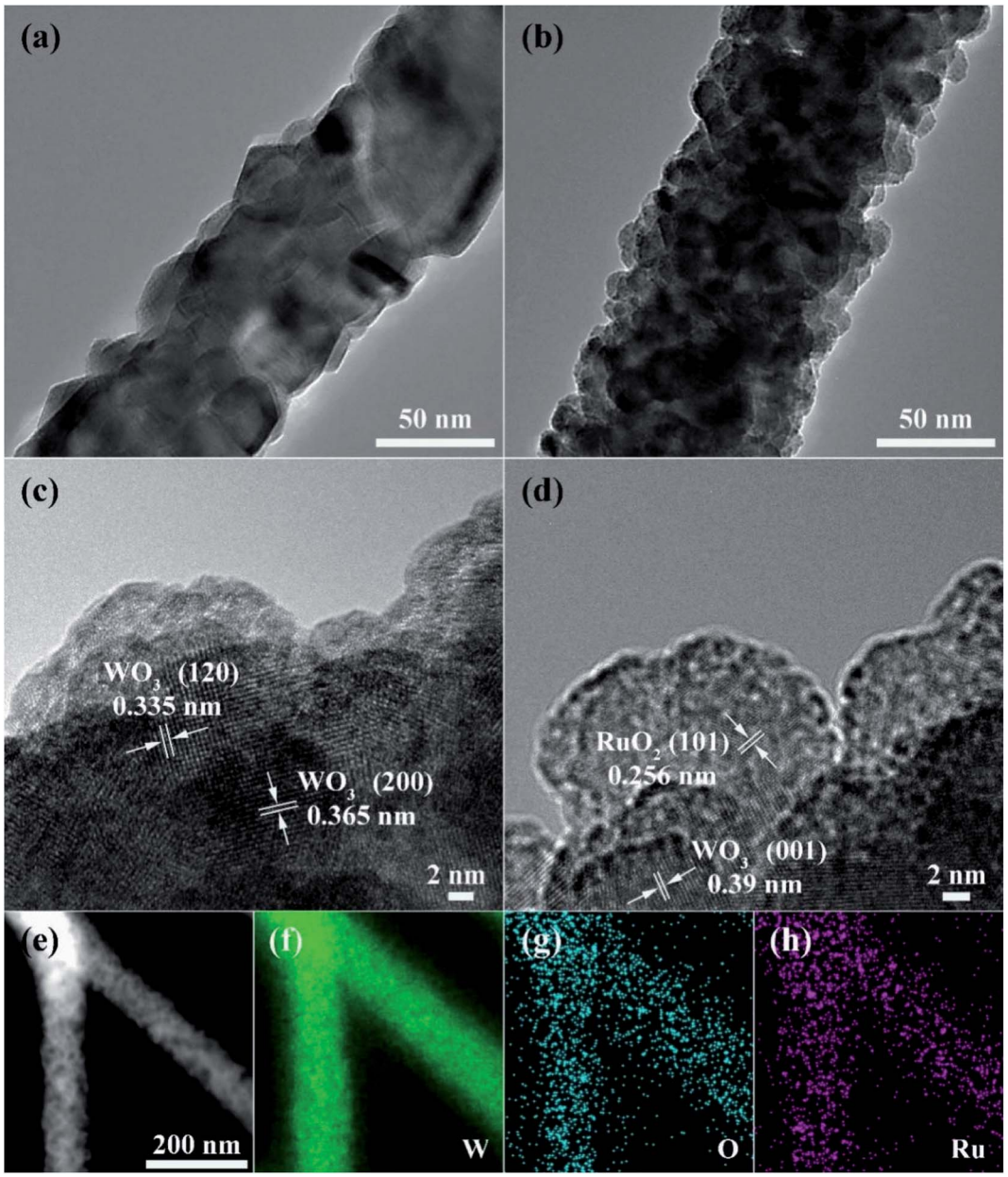

Fig. 4 TEM images of the (a) 0% Ru NWs and (b) 4% Ru NWs; (c and d) HRTEM images of the 4% Ru NWs; (e) STEM image and (f–h) corresponding element mapping images for the elements W, O, and Ru for the 4% Ru NWs.

increases in the range of 110–200 °C and decrease as the temperature increases further above 200 °C. Additionally, the response of the device based on the 0% Ru NW sample increases with temperature across the entire temperature range (as shown in the Fig. 5a inset), indicating that the optimum operating temperature of WO_3 can be reduced by introducing catalytic Ru.[51] The sensor based on 4% Ru NWs possesses the highest response to 100 ppm ethanol (120) at 200 °C, which is about 47 times higher than that of the sensor based on 0% Ru NWs under the same condition. This illustrates that decoration with Ru is a feasible method for enhancing the sensing performance of sensors based on WO_3 NWs towards ethanol.

Fig. 5b shows the dynamic response–recovery curves of the sensors towards 100 ppm ethanol at 200 °C. It is obvious that all the sensors based on Ru-decorated samples have an excellent response and recovery performance. Fig. S1a–j† displays the real-time curves of the variation of the sensor resistance at different temperatures in response to 100 ppm ethanol gas, which exhibit a classic n-type gas response phenomenon for n-type WO_3 in the detection of reducing gases. The resistance of the devices changes more rapidly due to quicker adsorption and desorption of ethanol at high temperatures compared to low temperatures. Furthermore, the resistance can be restored to its original level at any temperature. The τ_{res} and τ_{rec} of the sensors based on 0% Ru NWs towards 100 ppm ethanol at 200 °C

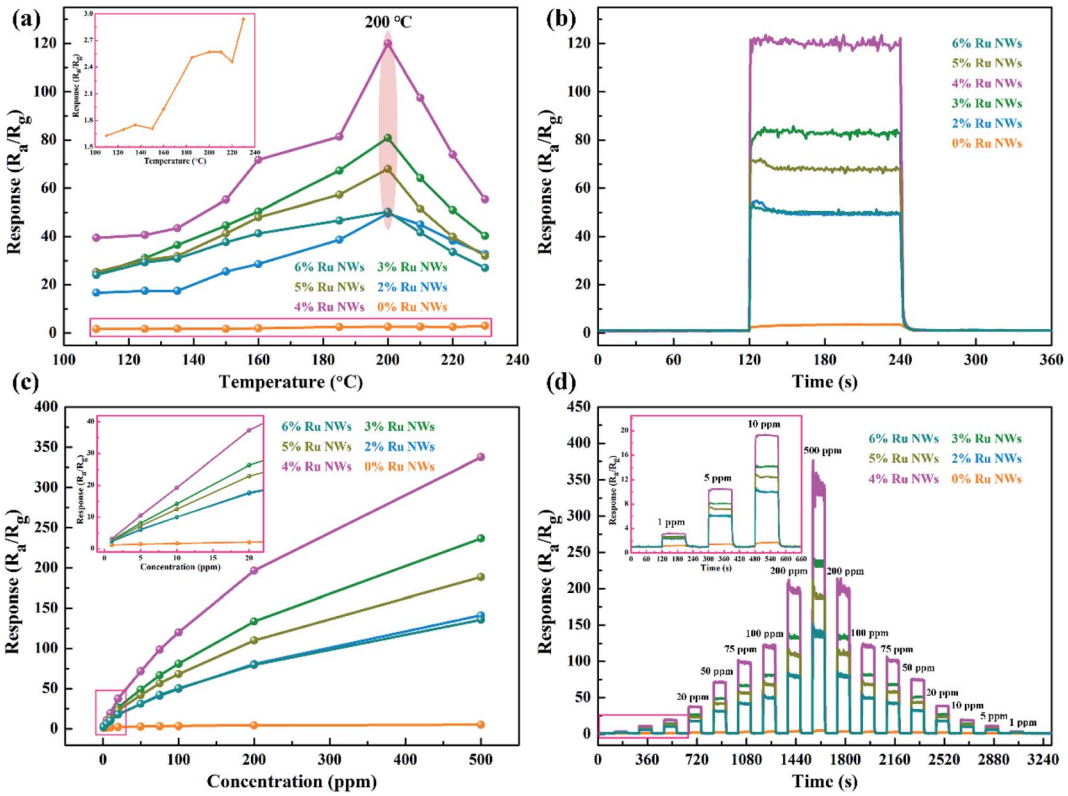

Fig. 5 (a) The responses of the samples towards 100 ppm ethanol as a function of operating temperature; the inset corresponds to the device based on 0% Ru NWs. (b) The dynamic response–recovery curves of the samples towards 100 ppm ethanol at 200 °C. (c) Curves of the responses toward various concentrations (1, 5, 10, 20, 50, 75, 100, 200, and 500 ppm) of ethanol gas for the samples. (d) The dynamic response–recovery curves of the sensors towards concentrations of ethanol of up to 500 ppm followed by down to 1 ppm; the inset corresponds to a low concentration (1–20 ppm) at 200 °C.

obtained from Fig. S1k and l† are 23 s and 58 s, and the corresponding values for the sensor based on 4% Ru NWs are 1 s and 18 s, respectively. This enhanced performance is ascribed to the catalytic effect of Ru, which promotes the chemical reaction between the target gas and adsorbed oxygen as well as the desorption of ethanol.[54] Fig. S2† shows the baseline resistance of sensors at various temperatures under air; it can be found that the resistance value decreases with increasing temperature, which is a typical characteristic of semiconductor materials. The resistance values of the sensors based on Ru-decorated WO_3 NWs are larger than those of the sensor based on the pure WO_3 NWs, which is ascribed to the widening of the depletion layer caused by the transition of electrons from the MOS to the noble metal. The sensing performance of the sensors in this work is compared to that of previously reported materials based on WO_3 in Table 1. These Ru-decorated WO_3 NWs evidently display outstanding sensing performance towards ethanol, with the best response among the compared materials and a lower optimum working temperature.

Table 1 Comparison of previous works and this work in terms of ethanol gas sensing performance[a]

Sample	T_{op} (°C)	Conc. (ppm)	Response (S)	Ref.
Core–shell WO_3–SnO_2 nanofibers	280	10	5.09	55
WO_3–SnO_2 composite coating	250	300	1.73	56
Ce-doped WO_3	350	1	12.3	57
$WO_3 \cdot H_2O$ network	350	100	16	25
Ga_2O_3–WO_3 heterostructures	275	100	14	58
Au-decorated WO_3	200	100	57	59
ZnO–WO_3 composite nanorods	300	50	16.2	60
Ru-decorated WO_3	200	100	78	This work

[a] T_{op}: optimum working temperature of the sensors.

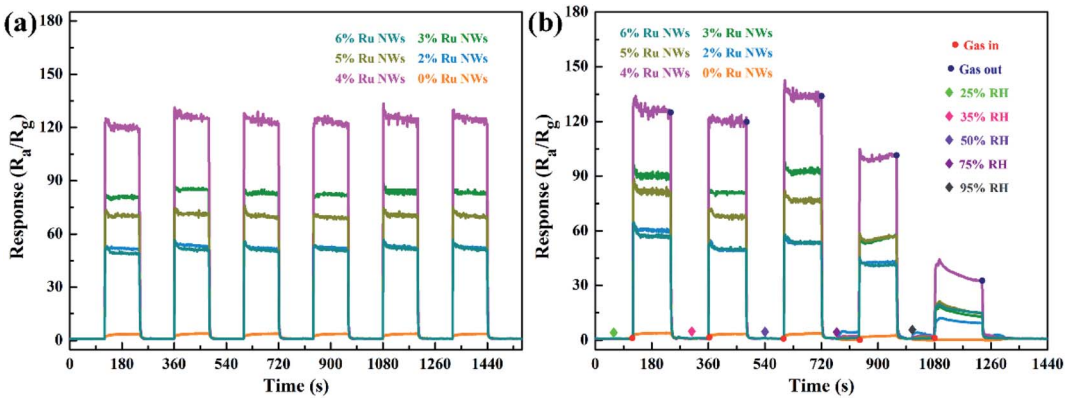

Fig. 6 (a) Repeatability test of the dynamic response curves of the sensors over six cycles, and (b) the dynamic response curves of the sensors under different RH (%) towards 100 ppm ethanol at 200 °C.

The response values of all the devices as a function of ethanol concentration (from 1 to 500 ppm) at their optimal working temperature are shown in Fig. 5c. As can be seen, the response values of the sensors increase with increasing ethanol concentration, and the worst sensing performance is achieved using the sensors based on the 0% Ru NW sample. In contrast, the 4%-Ru-NW-based sensor displays an outstanding response. Additionally, the response of the sensor based on 0% Ru NWs only increases slightly when the concentration of ethanol gas is increased, while the responses of the sensors based on Ru-decorated NWs increase rapidly. Importantly, the response value increases almost linearly at low ethanol concentrations (1–20 ppm), and there is no saturation trend as the ethanol concentration increases to 500 ppm. Furthermore, the dynamic response and recovery curves and corresponding ethanol response as a function of concentration for every sensor are shown in Fig. 5d and S3a,† and demonstrate good symmetry when the ethanol concentration is increased and then decreased. Additionally, Fig. S3b† shows the relationship between $\ln(S)$ and $\ln(C)$ at the optimum sensor working temperature. The experimental data can be fitted well by a linear function, and show that the ethanol detection limit was 759 ppb, 290 ppb, 257 ppb, 211 ppb, 270 ppb and 303 ppb, respectively, for the sensor devices based on the 0%, 2%, 3%, 4%, 5%, and 6% Ru NW materials.

When a varying amount of ethanol gas is injected, the response is immediate and quickly achieves stability. The resistance returns to its previous level when the devices are exposed to air, even for an ethanol concentration of 1 ppm. Fig. 6a shows six response cycles towards 100 ppm ethanol at 200 °C. There is a slight increase in the response, which is ascribed to the surfaces of the materials being activated by ethanol. The result illustrates the outstanding repeatability and reproducibility of these sensors. Overall, these results prove that the sensors have the potential to sensitively detect ethanol across a wide range of practical conditions.

Moisture negatively affects gas sensors,[18] so the effect of increasing humidity was investigated in this work. Fig. 6b displays the dynamic response curves of sensors exposed to ethanol under different RH conditions (25%, 35%, 50%, 75%, and 95%). There is only a slight change in the gas response even at 75% RH, although the sensors show better performance when the RH is 50%. The resistance of the devices slowly increases in a stable manner when the sensors are tested in a 95% RH environment. This is because water molecules occupy the gas and oxygen reaction sites, inhibiting the response. Such humidity effects are acceptable for practical application.

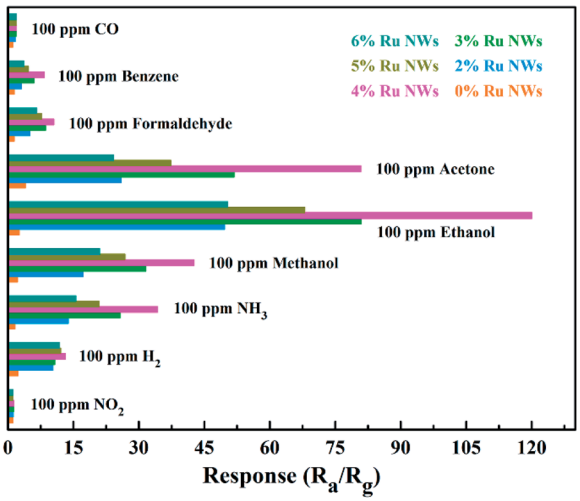

Fig. 7 Selectivity patterns of the sensors towards various gases (100 ppm benzene, formaldehyde, acetone, methanol, NH_3, CO, NO_2, H_2, and ethanol) at 200 °C.

Selectivity is also a crucial factor for the practical application of sensor devices. The response of all the sensors exposed to 100 ppm of the gases CO, NH_3, benzene, acetone, methanol, formaldehyde, NO_2, and H_2 were analyzed and are displayed in Fig. 7. The Ru-decorated sensors clearly demonstrate better sensing performance of all the VOC gases compared to the 0% Ru NWs sensor. Compared with their response to other gases, the sensors display optimal performance for the detection of ethanol. The sensor offers decent selectivity between ethanol

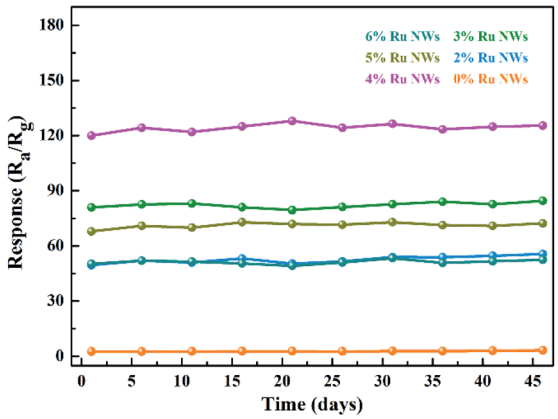

Fig. 8 Long-term stability of sensors towards 100 ppm ethanol at 200 °C.

and CO, benzene, formaldehyde, and NO_2. However, the selectivity towards ethanol over acetone, methanol and ammonia is not as satisfactory. The selectivity towards acetone is unsatisfactory, which is ascribed to the fact that the samples without Ru modification showed the best sensing performance towards acetone. The introduction of Ru can effectively break C–C bonds in VOCs, and the ethoxy species of ethanol are always present as monodentates with their oxygen atom bound to one Ru atom. Thus, the sensors based on Ru-decorated materials show the highest response to ethanol, while their sensing performance toward other VOCs is also enhanced. The statistics of the initial resistance for the sensor selectivity and repeatability tests (Fig. S4†) illustrates that the devices can almost completely recover after exposure to the tested gases, further demonstrating the outstanding repeatability of the sensors.

Gas sensors based on MOS are always limited in practical application by poor long-term stability performance; therefore, more stable sensor materials are required. As shown in Fig. 8 and S5,† the prepared sensors based on WO_3 NWs demonstrate extremely stable performance for practical ethanol detection. The sensing performance is even slightly increased after 45 days, and the dynamic response and recovery curves have the same characteristics, as shown in Fig. 6a. In brief, these sensors have good moisture resistance, selectivity and long-term stability.

3.3 Mechanism

The resistance value of the sensors is stable in conditions where air is the background due to a dynamic equilibrium between the oxygen adsorption and desorption processes. Currently, the widely accepted sensing mechanism of typical n-type MOS (WO_3) materials for the detection of reducing gases (ethanol) is attributed to the change in carrier concentration due to the capture and release of electrons during the chemical reaction between the target gas and the oxygen species adsorbed on the MOS surface.[33,61] Therefore, the movement of electrons and the

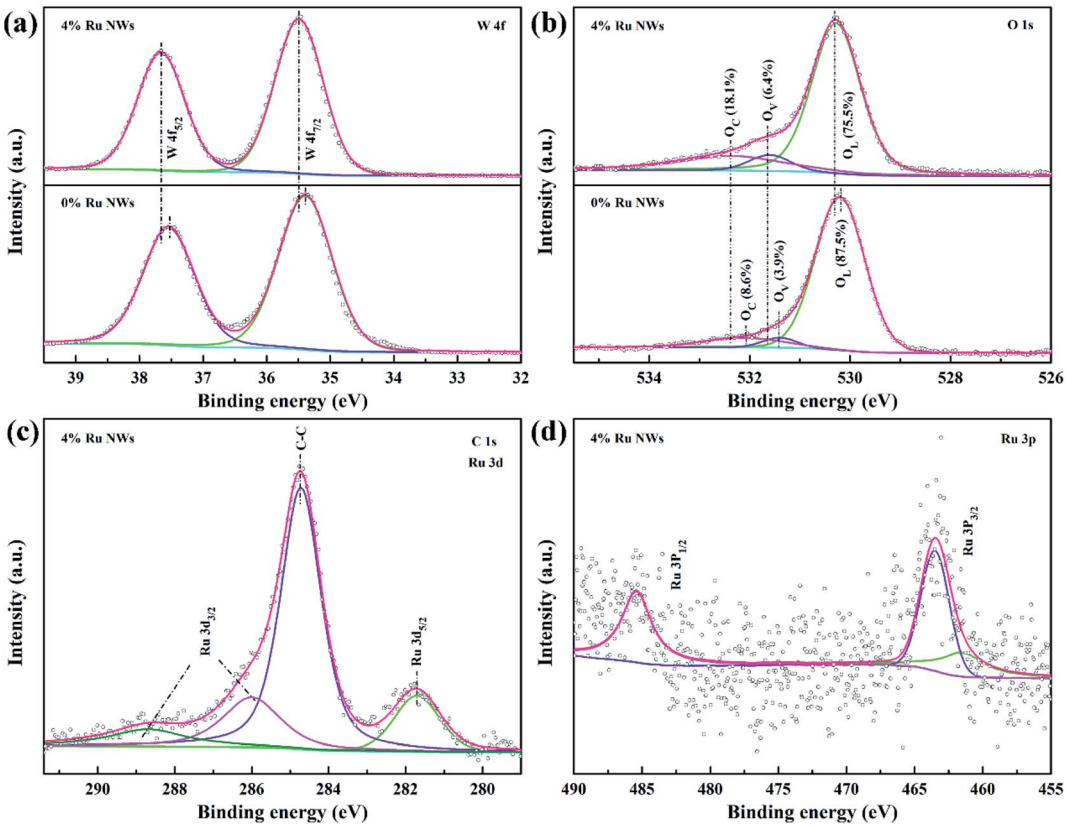

Fig. 9 (a) W 4f, (b) O 1s XPS spectra of 0% Ru NWs, and 4% Ru NWs samples, (c) Ru 3d and (d) Ru 3p spectra of 4% Ru NWs samples.

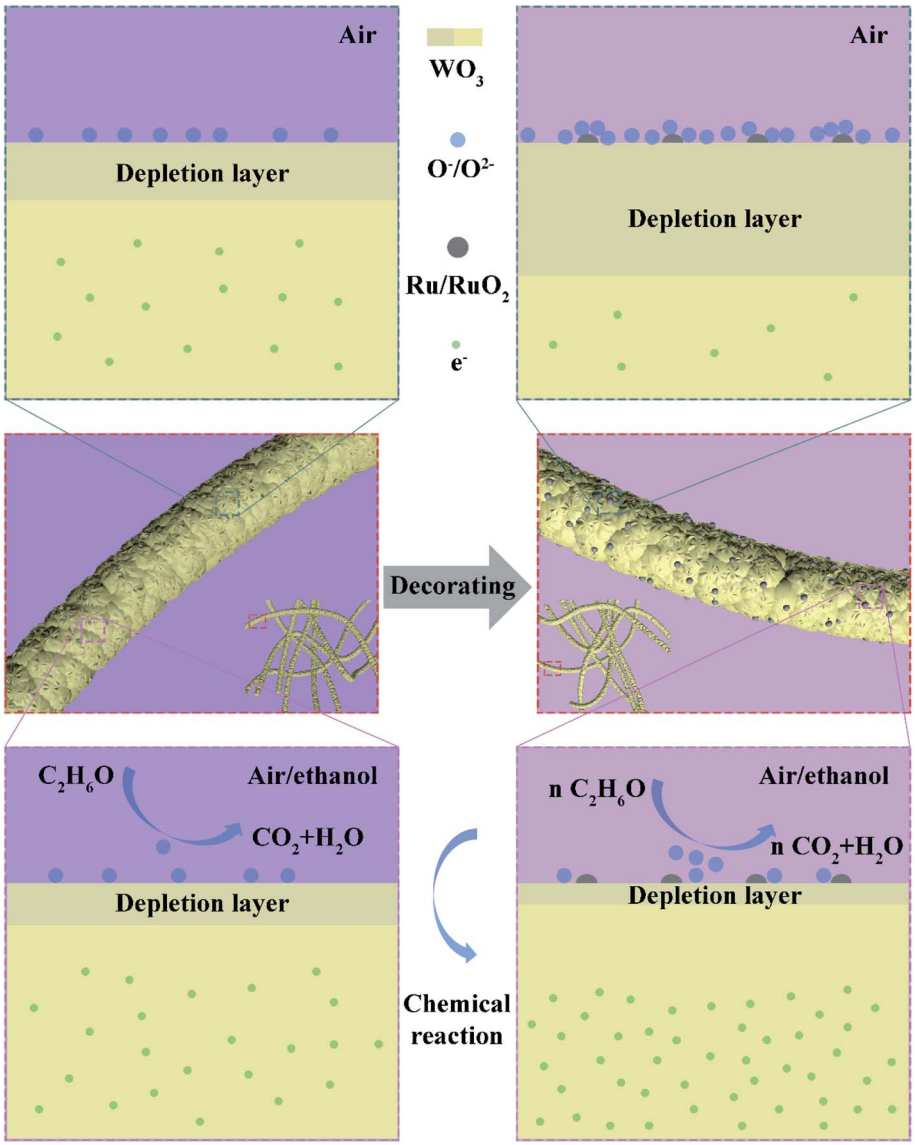

Fig. 10 Schematic diagram of pure and Ru-decorated WO_3 NWs and their ethanol sensing mechanism and its enhancement.

changes in adsorbed oxygen species on the surface of the materials when the sensors are exposed to alternating atmospheres under a certain concentration of the target gas should be investigated. The conduction band electrons can be trapped by oxygen to form chemisorbed oxygen species; this process is highly dependent on the working temperature in air ($O_{2\ (ads)} + 2e^- \leftrightarrow 2O^-_{(ads)}$ ($100\ ^\circ C < T < 300\ ^\circ C$)).[22] The trapped electrons are released back to the conduction band with the introduction of reducing gas (the gas will undergo an oxidation–reduction reaction with the adsorbed oxygen, releasing electrons to participate in conduction).[28] As a result, an electron depletion layer is formed on the surface of the sensing materials in air, and the width of this depletion layer is reduced in testing; this leads to the change in the resistance of the sensing materials, consistent with Fig. S1.†

The improvement in the sensing performance can be explained by the electronic and chemical sensitization of Ru. The 0% Ru NW and 4% Ru NW samples were characterized using XPS (Fig. S6† and 9) to analyze the chemical states of elements (W, O, and Ru) and the sample compositions. The comparison of the full survey spectra shown in Fig. S6† clearly shows a weak peak at around 282 eV and a slight change at around 463 eV for the Ru-decorated sample, corresponding to Ru 3d and Ru 3p, respectively. The Ru 3p peak, which is only present in the 4% Ru NWs samples, illustrates the presence of Ru. The high-resolution spectra of W 4f, O 1s, Ru 3d, and Ru 3p are shown in Fig. 9a–d. Fig. 9a displays two peaks at 35.5 ± 0.1 eV (W $4f_{7/2}$) and 37.6 ± 0.1 eV (W $4f_{5/2}$), corresponding to the W^{6+} oxidation state. In the O 1s XPS spectrum in Fig. 9b, there are three major peaks located at 530.25 ± 0.1 eV, 531.5 ± 0.1 eV, and 532.2 ± 0.1 eV, which are respectively ascribed to lattice oxygen (O_L), oxygen vacancies (O_V), and chemisorbed oxygen (O_C) on the WO_3 surface.

Decorating the WO_3 NWs with 4% Ru increases the amount of O_V from 3.9% to 6.4%, providing more reaction sites for target gases, and increases O_C from 8.6% to 18.1%, indicating that more chemisorbed oxygen can participate in the chemical reaction.[36] This explains the larger response of the Ru-decorated WO_3. Additionally, as shown in Fig. 9c, the XPS peaks of Ru 3d overlap with the C 1s peak. The peaks located at 281.7 eV and around 286 eV correspond to Ru $3d_{5/2}$ and Ru $3d_{3/2}$. The Ru 3p XPS spectrum displayed in Fig. 9d illustrates that ruthenium is in the form of RuO_2.[62] Importantly, both the W 4f and O 1s peaks of the 4% Ru NWs spectrum shift to higher binding energy positions, indicating that the electron migration direction between WO_3 and Ru is from the semiconductor to the noble metal. This leads to a higher resistance state of the devices based on the Ru-decorated samples, in line with Fig. S1 and S2.† This also proves the interaction between Ru and WO_3. Their synergy is conducive to the improvement of the sensing performance. In addition, RuO_2 is a p-type MOS; therefore, a p–n heterojunction is formed at the interface between RuO_2 and WO_3. Additionally, the work function of RuO_2 is higher than that of WO_3, so electrons will migrate from WO_3 to RuO_2 until their Fermi levels are balanced.[63] This widens the electron depletion layer, which is beneficial for enhancing the sensitivity of WO_3. Because a lower electron concentration means a higher baseline resistance of the sensors in air, this results in a higher response based on the equation $S = R_a/R_g$. The ethanol sensing mechanism and enhancement for pure and Ru-decorated samples are shown in Fig. 10.

The devices based on Ru-decorated samples have a lower optimal operating temperature and faster response and recovery. This is ascribed to the catalytic effect of RuO_2, which reduces the activation energy of the gas to react with adsorbed oxygen and accelerates the dynamic equilibrium of the oxygen adsorption and desorption processes. The gas sensing property of the samples improves with increasing Ru decoration up to 4 at%. Above this, the gas sensing property deteriorates, which can be explained by the lower atom utilization efficiency under the same conditions.[64] The stability of these sensors is attributed to the nature of the WO_3 NWs. The materials were annealed at 500 °C during the preparation process, and the sensors underwent a high-temperature aging treatment, enhancing material stability.

4 Conclusions

In summary, various amounts of the noble metal Ru were used to functionalize the surface of WO_3 NWs prepared by a traditional electrospinning method *via* a facile and low-cost UV irradiation process. In particular, the sensor device based on 4% Ru-decorated WO_3 NWs achieves the most outstanding performance for ethanol detection at a low working temperature of 200 °C, with a response 47 times higher than that of undecorated WO_3 NWs. The response of the prepared sensors to step changes in the concentration of ethanol is clearly distinguished. The lowest detection limit level is 221 ppb. Furthermore, these sensors exhibit good repeatability and stability even after 45 days or under high relative humidity conditions. This can be ascribed to the higher level of oxygen vacancies and surface chemically adsorbed oxygen species on the Ru-decorated WO_3 caused by the electronic/chemical sensitization effect of Ru, the catalytic effect of RuO_2, the optimized atomic utilization efficiency, and the heterojunction formed at the interface between WO_3 and RuO_2. Overall, this work clearly proves that using Ru to decorate the surface of a MOS is an effective and promising method for promoting ethanol sensing performance.

Author contributions

Jianjun Li: conceptualization, methodology, formal analysis, validation, data curation, writing—original draft, writing—review & editing. Qiongling Ding: methodology. Xichao Mo: data collection, investigation. Zihao Zou: data collection, investigation. Pu Cheng: data collection. Yiding Li: data collection. Kai Sun: data collection. Yujun Fu: data collection, supervision. Yanrong Wang: conceptualization, methodology, funding acquisition, writing—original draft, writing—review & editing, supervision. Deyan He: conceptualization, supervision. All authors have read and agreed to the published version of the manuscript.

Conflicts of interest

The authors declare no competing interest.

Acknowledgements

This work was supported by the National Natural Science Foundation of China (No. 61801200), and the Fundamental Research Funds for the Central Universities (No. lzujbky-2020-60).

References

1 Y. Wang, P. Cheng, X. Li, C. Wang, C. Feng and G. Lu, Revealing the relationship between the Au decoration method and the enhanced acetone sensing performance of a mesoporous In_2O_3-based gas sensor, *J. Mater. Chem. C*, 2020, **8**, 78–88.

2 A. Staerz, S. Somacescu, M. Epifani, T. Kida, U. Weimar and N. Barsan, WO_3-based gas sensors: identifying inherent qualities and understanding the sensing mechanism, *ACS Sens.*, 2020, **5**, 1624–1633.

3 K. Xu, N. Liao, B. Zheng and H. Zhou, Adsorption and diffusion behaviors of H_2, H_2S, NH_3, CO and H_2O gases molecules on MoO_3 monolayer: A DFT study, *Phys. Lett. A*, 2020, **384**, 126533.

4 H. Yu, J. Li, Z. Li, Y. Tian and Z. Yang, Enhanced formaldehyde sensing performance based on Ag@WO_3 2D nanocomposite, *Powder Technol.*, 2019, **343**, 1–10.

5 Z. Zhu, C.-T. Kao and R.-J. Wu, A highly sensitive ethanol sensor based on Ag@TiO_2 nanoparticles at room temperature, *Appl. Surf. Sci.*, 2014, **320**, 348–355.

6 T. Tesfamichael, Electron beam evaporation of tungsten oxide films for gas sensors, *IEEE Sens. J.*, 2010, **10**, 1796–1802.
7 J. Yang and Y. S. Lin, Design of tunable terahertz metamaterial sensor with single- and dual-resonance characteristic, *Nanomaterials*, 2021, **11**, 2221.
8 Z. Liang, Y. Wen, Z. Zhang, Z. Liang, Z. Xu and Y.-S. Lin, Plasmonic metamaterial using metal-insulator-metal nanogratings for high-sensitive refraction index sensor, *Results Phys.*, 2019, **15**, 102602.
9 J. Zhong, X. Xu and Y. S. Lin, Tunable terahertz metamaterial with electromagnetically induced transparency characteristic for sensing application, *Nanomaterials*, 2021, **11**, 2175.
10 Y. Zhang, P. Lin and Y. S. Lin, Tunable split-disk metamaterial absorber for sensing application, *Nanomaterials*, 2021, **11**, 598.
11 Z. Lin, Z. Xu, P. Liu, Z. Liang and Y.-S. Lin, Polarization-sensitive terahertz resonator using asymmetrical F-shaped metamaterial, *Opt. Laser Technol.*, 2020, **121**, 105826.
12 Y.-S. Lin, Complementary infrared metamaterials for volatile organic solutions sensing, *Mater. Lett.*, 2017, **195**, 55–57.
13 Y. Wen, Z. Liang and Y.-S. Lin, Tunable perfect meta-absorber with high-sensitive polarization characteristic, *Advanced Photonics Research*, 2020, **2**, 2000027.
14 H. Zhang, H. Li, L. Cai, Q. Lei, J. Wang, W. Fan, *et al.*, Performances of In-doped CuO-based heterojunction gas sensor, *J. Mater. Sci.: Mater. Electron.*, 2019, **31**, 910–919.
15 Y. Wang, Z. Zhao, Y. Sun, P. Li, J. Ji, Y. Chen, *et al.*, Fabrication and gas sensing properties of Au-loaded SnO_2 composite nanoparticles for highly sensitive hydrogen detection, *Sens. Actuators, B*, 2017, **240**, 664–673.
16 D. Zhang, Y. Cao, Z. Yang and J. Wu, Nanoheterostructure construction and DFT study of Ni-Doped In_2O_3 nanocubes/WS_2 hexagon nanosheets for formaldehyde sensing at room temperature, *ACS Appl. Mater. Interfaces*, 2020, **12**, 11979–11989.
17 J. M. Xu and J. P. Cheng, The advances of Co_3O_4 as gas sensing materials: A review, *J. Alloys Compd.*, 2016, **686**, 753–768.
18 C. Zhang, S. Zhang, Y. Yang, H. Yu and X. Dong, Highly sensitive H_2S sensors based on metal-organic framework driven γ-Fe_2O_3 on reduced graphene oxide composites at room temperature, *Sens. Actuators, B*, 2020, **325**, 128804.
19 Z. Wang, Z. Tian, D. Han and F. Gu, Au-modified three-dimensionally ordered macroporous ZnO:In for high-performance ethanol sensors, *J. Mater. Chem. C*, 2020, **8**, 2812–2819.
20 T. P. Mokoena, Z. P. Tshabalala, K. T. Hillie, H. C. Swart and D. E. Motaung, The blue luminescence of p-type NiO nanostructured material induced by defects: H_2S gas sensing characteristics at a relatively low operating temperature, *Appl. Surf. Sci.*, 2020, **525**, 146002.
21 X. Chang, S. Xu, S. Liu, N. Wang, S. Sun, X. Zhu, *et al.*, Highly sensitive acetone sensor based on WO_3 nanosheets derived from WS_2 nanoparticles with inorganic fullerene-like structures, *Sens. Actuators, B*, 2021, **343**, 130135.
22 Q. Ding, Y. Wang, P. Guo, J. Li, C. Chen, T. Wang, *et al.*, Cr-doped urchin-like WO_3 hollow spheres: the cooperative modulation of crystal growth and energy-band structure for high-sensitive acetone detection, *Sensors*, 2020, **20**, 3473.
23 H. Gao, Y. Ma, P. Song, Z. Yang and Q. Wang, Cu-doped Fe_2O_3 porous spindles derived from metal-organic frameworks with enhanced sensitivity to triethylamine, *Mater. Sci. Semicond. Process.*, 2021, **123**, 105510.
24 Y.-S. Lin and W. Chen, A large-area, wide-incident-angle, and polarization-independent plasmonic color filter for glucose sensing, *Opt. Mater.*, 2018, **75**, 739–743.
25 S. Liu, W. Zeng and Y. Li, Synthesis of spherical $WO_3 \cdot H_2O$ network for ethanol sensing application, *Mater. Lett.*, 2019, **253**, 42–45.
26 D. Zhang, Y. Cao, J. Wu and X. Zhang, Tungsten trioxide nanoparticles decorated tungsten disulfide nanoheterojunction for highly sensitive ethanol gas sensing application, *Appl. Surf. Sci.*, 2020, **503**, 144063.
27 Q. Li, D. Chen, J. Miao, S. Lin, Z. Yu, D. Cui, *et al.*, Highly sensitive sensor based on ordered porous ZnO nanosheets for ethanol detecting application, *Sens. Actuators, B*, 2021, **326**, 128952.
28 C. Dong, R. Zhao, L. Yao, Y. Ran, X. Zhang and Y. Wang, A review on WO_3 based gas sensors: morphology control and enhanced sensing properties, *J. Alloys Compd.*, 2020, **820**, 153194.
29 J. Qi, K. Chen, Y. Xing, H. Fan, H. Zhao, J. Yang, *et al.*, Application of 3D hierarchical monoclinic-type structural Sb-doped WO_3 towards NO_2 gas detection at low temperature, *Nanoscale*, 2018, **10**, 7440–7450.
30 L. Deng, X. Ding, D. Zeng, S. Zhang and C. Xie, High sensitivity and selectivity of C-doped WO_3 gas sensors toward toluene and xylene, *IEEE Sens. J.*, 2012, **12**, 2209–2214.
31 Y. Zeng, Z. Hua, X. Tian, X. Li, Z. Qiu, C. Zhang, *et al.*, Selective detection of methanol by zeolite/Pd-WO_3 gas sensors, *Sens. Actuators, B*, 2018, **273**, 1291–1299.
32 Z. Qiu, Z. Hua, Y. Li, M. Wang, D. Huang, C. Tian, *et al.*, Acetone sensing properties and mechanism of Rh-loaded WO_3 Nanosheets, *Front. Chem.*, 2018, **6**, 385.
33 J. Dai, O. Ogbeide, N. Macadam, Q. Sun, W. Yu, Y. Li, *et al.*, Printed gas sensors, *Chem. Soc. Rev.*, 2020, **49**, 1756–1789.
34 K. T. Alali, J. Liu, K. Aljebawi, P. Liu, R. Chen, R. Li, *et al.*, Electrospun n-p WO_3/CuO heterostructure nanofibers as an efficient sarin nerve agent sensing material at room temperature, *J. Alloys Compd.*, 2019, **793**, 31–41.
35 H. Shao, M. Huang, H. Fu, S. Wang, L. Wang, J. Lu, *et al.*, Hollow WO_3/SnO_2 hetero-nanofibers: controlled synthesis and high efficiency of acetone vapor detection, *Front. Chem.*, 2019, **7**, 785.
36 J. Lu, C. Xu, L. Cheng, N. Jia, J. Huang and C. Li, Acetone sensor based on WO_3 nanocrystallines with oxygen defects for low concentration detection, *Mater. Sci. Semicond. Process.*, 2019, **101**, 214–222.
37 S. Kabcum, N. Kotchasak, D. Channei, A. Tuantranont, A. Wisitsoraat, S. Phanichphant, *et al.*, Highly sensitive

and selective NO_2 sensor based on Au-impregnated WO_3 nanorods, *Sens. Actuators, B*, 2017, **252**, 523–536.

38 A. Nikfarjam, S. Fardindoost and A. Iraji zad, Fabrication of Pd doped WO_3 nanofiber as hydrogen sensor, *Polymers*, 2013, **5**, 45–55.

39 C.-H. Chang, T.-C. Chou, W.-C. Chen, J.-S. Niu, K.-W. Lin, S.-Y. Cheng, *et al.*, Study of a WO_3 thin film based hydrogen gas sensor decorated with platinum nanoparticles, *Sens. Actuators, B*, 2020, **317**, 128145.

40 P. V. Morais, P. H. Suman, R. A. Silva and M. O. Orlandi, High gas sensor performance of WO_3 nanofibers prepared by electrospinning, *J. Alloys Compd.*, 2021, **864**, 158745.

41 S. J. Choi, S. Chattopadhyay, J. J. Kim, S. J. Kim, H. L. Tuller, G. C. Rutledge, *et al.*, Coaxial electrospinning of WO_3 nanotubes functionalized with bio-inspired Pd catalysts and their superior hydrogen sensing performance, *Nanoscale*, 2016, **8**, 9159–9166.

42 P. P. Mane, R. S. Ambekar and B. Kandasubramanian, Electrospun nanofiber-based cancer sensors: A review, *Int. J. Pharm.*, 2020, **583**, 119364.

43 G. Korotcenkov, Electrospun metal oxide nanofibers and their conductometric gas sensor application. Part 2: gas sensors and their advantages and limitations, *Nanomaterials*, 2021, **11**, 1555.

44 P. Su, W. Pei, X. Wang, Y. Ma, Q. Jiang, J. Liang, *et al.*, Exceptional electrochemical HER performance with enhanced electron transfer between Ru nanoparticles and single atoms dispersed on a carbon substrate, *Angew. Chem., Int. Ed. Engl.*, 2021, **60**, 16044–16050.

45 M. Gao, H. Tan, P. Zhu, J. Zhang, H. Wang, X. Liu, *et al.*, Why phenol is selectively hydrogenated to cyclohexanol on Ru (0001): an experimental and theoretical study, *Appl. Surf. Sci.*, 2021, **558**, 149880.

46 H. P. Pacheco, E. F. de Souza, S. M. Landi, M. V. David, J. Tyler Prillaman, R. J. Davis, *et al.*, Ru Promoted MgO and Al-Modified MgO for Ethanol Upgrading, *Top. Catal.*, 2019, **62**, 894–907.

47 A. Rodríguez-Gómez, E. Lepre, L. Sánchez-Silva, N. López-Salas and A. R. de la Osa, PtRu nanoparticles supported on noble carbons for ethanol electrooxidation, *J. Energy Chem.*, 2022, **66**, 168–180.

48 L. Wei, F. Liu, X. Jiang, Y.-H. Yang, T. Sheng, Q.-Q. Xu, *et al.*, High-index faceted Pt-Ru alloy concave nanocubes with enhancing ethanol and CO electro-oxidation, *Electrochim. Acta*, 2021, **396**, 139266.

49 A. Waheed, X. Wang, N. Maeda, S. Naito and A. Baiker, Surface processes occurring during aqueous phase ethanol reforming on Ru/TiO_2 tracked by ATR-IR spectroscopy, *Appl. Catal., A*, 2019, **581**, 111–115.

50 D. Huang, W. Yuan, S. Fan, C. Tian, Z. Hua, X. Tian, *et al.*, Hydrogen sensing mechanism of Ru-loaded WO_3 nanosheets, *Sens. Actuators, B*, 2020, **304**, 127339.

51 Y. Li, Z. Hua, Y. Wu, Y. Zeng, Z. Qiu, X. Tian, *et al.*, Modified impregnation synthesis of Ru-loaded WO_3 nanoparticles for acetone sensing, *Sens. Actuators, B*, 2018, **265**, 249–256.

52 H. Li, S. Chu, Q. Ma, J. Wang, Q. Che, G. Wang, *et al.*, Hierarchical $WO_3/ZnWO_4$ 1D fibrous heterostructures with tunable *in situ* growth of WO_3 nanoparticles on surface for efficient low concentration HCHO detection, *Sens. Actuators, B*, 2019, **286**, 564–574.

53 X. Kou, F. Meng, K. Chen, T. Wang, P. Sun, F. Liu, *et al.*, High-performance acetone gas sensor based on Ru-doped SnO_2 nanofibers, *Sens. Actuators, B*, 2020, **320**, 128292.

54 S. S. Mehta, D. Y. Nadargi, M. S. Tamboli, L. S. Chaudhary, P. S. Patil, I. S. Mulla, *et al.*, Ru-loaded mesoporous WO_3 microflowers for dual applications: enhanced H_2S sensing and sunlight-driven photocatalysis, *Dalton Trans.*, 2018, **47**, 16840–16845.

55 F. Li, X. Gao, R. Wang and T. Zhang, Design of WO_3-SnO_2 core-shell nanofibers and their enhanced gas sensing performance based on different work function, *Appl. Surf. Sci.*, 2018, **442**, 30–37.

56 V. Ambardekar, P. P. Bandyopadhyay and S. B. Majumder, Understanding on the ethanol sensing mechanism of atmospheric plasma sprayed 25 wt. % WO_3-75 wt. % SnO_2 coating, *Sens. Actuators, B*, 2019, **290**, 414–425.

57 Q. Diao, Y. Yin, W. Jia, X. Xu, Y. Ding, X. Zhang, *et al.*, Highly sensitive ethanol sensor based on Ce-doped WO_3 with raspberry-like architecture, *Mater. Res. Express*, 2020, **7**, 115012.

58 Z. Wei, M. K. Akbari, Z. Hai, R. K. Ramachandran, C. Detavernier, F. Verpoort, *et al.*, Ultra-thin sub-10nm Ga_2O_3-WO_3 heterostructures developed by atomic layer deposition for sensitive and selective $C_2H_5O_H$ detection on ppm level, *Sens. Actuators, B*, 2019, **287**, 147–156.

59 J. Ma, X. Xiao, Y. Zou, Y. Ren, X. Zhou, X. Yang, *et al.*, A general and straightforward route to noble metal-decorated mesoporous transition-metal oxides with enhanced gas sensing performance, *Small*, 2019, **15**, 1904240.

60 Y. C. Liang and C. W. Chang, Improvement of ethanol gas-sensing responses of ZnO-WO_3 composite nanorods through annealing induced local phase transformation, *Nanomaterials*, 2019, **9**, 669.

61 B. Yang, N. V. Myung and T. T. Tran, 1D metal oxide semiconductor materials for chemiresistive gas sensors: A Review, *Adv. Electron. Mater.*, 2021, 202100271.

62 P. Hao, P. Song, Z. Yang and Q. Wang, Synthesis of novel $RuO_2/LaFeO_3$ porous microspheres its gas sensing performances towards triethylamine, *J. Alloys Compd.*, 2019, **806**, 960–967.

63 C. Wang, S. Zhang, L. Qiu, S. A. Rasaki, F. Qu, T. Thomas, *et al.*, Ru-decorated WO_3 nanosheets for efficient xylene gas sensing application, *J. Alloys Compd.*, 2020, **826**, 154196.

64 L. Zhang, K. Doyle-Davis and X. Sun, Pt-based electrocatalysts with high atom utilization efficiency: from nanostructures to single atoms, *Energy Environ. Sci.*, 2019, **12**, 492–517.